The Meteoritical Society

Meteoritics & Planetary Science 43, Nr 1/2, 247–259 (2008)
Abstract available online at http://meteoritics.org

Bulk mineralogy and three-dimensional structures of individual Stardust particles deduced from synchrotron X-ray diffraction and microtomography analysis

Tomoki NAKAMURA[1*], Akira TSUCHIYAMA[2], Takeshi AKAKI[1], Kentaro UESUGI[3], Tsukasa NAKANO[4], Akihisa TAKEUCHI[3], Yoshio SUZUKI[3], and Takaaki NOGUCHI[5]

[1]Department of Earth and Planetary Science, Faculty of Science, Kyushu University, Hakozaki, Fukuoka 812-8581, Japan
[2]Department of Earth and Space Science, Graduate School of Science, Osaka University, Toyonaka 560-0043, Japan
[3]Japan Synchrotron Radiation Research Institute, SPring-8, Sayo, Hyogo 679-5198, Japan
[4]Geological Survey of Japan, Advanced Industrial Science and Technology, Tsukuba 305-8567, Japan
[5]Department of Materials and Biological Sciences, Ibaraki University, 2-1-1 Bunkyo, Mito 310-8512, Japan
*Corresponding author. E-mail: tomoki@geo.kyushu-u.ac.jp

(Submitted 29 March 2007; revision accepted 28 August 2007)

Abstract–During preliminary examination of particles released from 81P/Wild 2 short-period comet, we analyzed 28 particles by nondestructive means, high-sensitive X-ray diffraction and high-resolution X-ray tomography, in order to characterize bulk mineralogy and three-dimensional structures of individual particles. The analyses were performed at synchrotron facilities, KEK and SPring-8 in Japan. Twenty-eight particles from 5 to 25 μm in size, including 25 particles from Track 35 and 3 particles from Track 44, were first analyzed by X-ray diffraction and then 4 out of 28 particles were analyzed by X-ray tomography.

All particles are classified into two groups based on silicate crystallinity: crystalline type and amorphous-rich type. The abundance of the former is approximately 10% of the particles investigated. Crystalline type shows very sharp reflections of olivine and low-Ca pyroxene, while amorphous-rich type shows no or very weak silicate reflections, suggesting that silicates are mostly amorphous. Broad reflections of Fe sulfides and Fe silicides are detected from most of amorphous-rich type particles. Subsequent tomography analysis revealed that the crystalline type is non-porous material consisting of coarse silicate crystals larger than 1 μm in size, while the amorphous-rich type is very porous aggregates with amorphous silicates and small Fe sulfide and Fe metallic grains. All characteristics of amorphous-rich type particles indicate that most of them are melted and rapidly solidified during capture in the silica aerogel. On the other hand, the crystalline type is indigenous cometary particle formed through high-temperature heating episodes that have taken place prior to formation of comet Wild 2. One of the crystalline-type particles (C2054,0,35,6,0) consists of Mg-rich olivine, pyroxene, and kamacite and exhibits porphyritic or poikilitic texture very similar to chondrules.

INTRODUCTION

Comet 81P/Wild 2 is a member of the Jupiter family of comets that are believed to have formed at regions of the Kuiper belt in the beginning of our solar system. Solid particles swept out from the comet are thus old particles that preserve the records of solar system formation. The Stardust spacecraft succeeded in collecting thousands of solid particles from comet Wild 2 (Brownlee et al. 2006), but the sizes of the particles are very small, ranging from submicron to 30 μm, comparable to or even smaller than the size of the smallest extraterrestrial particles, interplanetary dust particles (IDPs), recovered on Earth. Characterization of such small particles requires multi-disciplinary analytical methods to maximize information derived from a single particle. As a part of a preliminary examination that was organized to characterize cometary particles (e.g., Brownlee et al. 2006; Zolensky et al. 2006), we performed completely non-destructive analysis by utilizing synchrotron radiation X-ray. The advantage of our methods is its capability to determine the mineral combination and the internal structure without any loss of precious samples. Other groups also utilize synchrotron tomography and XRF to investigate Stardust particles and earlier analogs (e.g., Flynn et al. 2006; Ebel et al. 2007). In this study, we succeeded to classify Wild 2 particles into two distinct categories based on mineralogical and structural data.

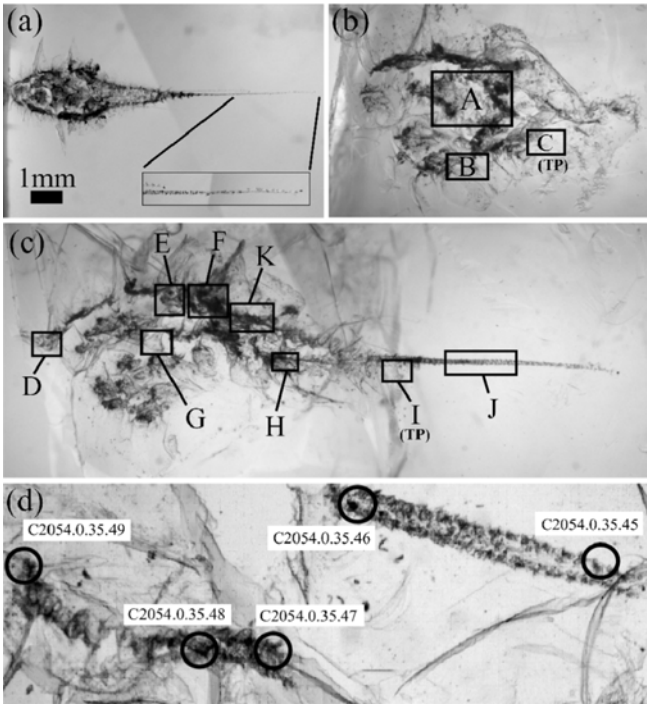

Fig. 1. Transmitted optical microscope images of Track 35. a) A whole view. A cometary particle came from the left side of the image and a final terminal particle stops at the right end. Inset is an enlarged view of a narrow track to the terminal particle. b) A whole view of a half portion of Track 35. The squares A, B, and C are the positions from which particles were extracted. The positions correspond to those referred to in Table 1. Terminal particle C2054,0,35,6,0 was extracted from a subtrack in position C. c) A whole view of another half portion of Track 35. Particles were extracted from various locations including positions close to the entrance hole, the middle and the bottom of the bulbous part, and along a track to the terminal particle. From a subtrack in position I, terminal particle C2054,11,35,62,0 was extracted. d) An enlarged view of the narrow track leading the way to the terminal particle, corresponding to the position J in (c). The track is broken and misaligned because it was pressed between Mylar sheets to extract particles.

EXPERIMENTAL PROCEDURES

Extraction of Particles from Silica Aerogel

Three particles were extracted from the hedgehog-shape Track 44 which is the largest impact feature on the cometary tray, based on the description of the Stardust catalog in the JSC website. The track is located on the cell C2004 and measures approximately 6 mm in entrance diameter and 8 mm in depth. A piece of aerogel was pulled out from the wall of the track by the curator (Dr. Zolensky) and three particles were separated from the aerogel. On the other hand, 25 particles were extracted from Track 35 located on the cell C2054 (Figs. 1a–d). The track was classified to type B track (Hörz et al. 2006). The track is also large, with approximately 1 mm entrance diameter and 11.8 mm in depth. It has a turnip shape. It was cut parallel to the traveling direction of an incoming particle and divided into two pieces (Figs. 1b and 1c). Less than four particles were extracted from each location in the track (Figs. 1b and 1c). The extracted particles included some terminal particles of subtracks, but most particles were taken from the wall of the main track. Four particles were extracted from a narrow tunnel to the largest terminal particle and the exact location of the four particles is shown in Fig. 1d. All operations were performed at the clean room for Stardust samples at NASA Johnson Space Center in February, March, and May 2007.

Synchrotron X-ray Diffraction

Each particle was mounted on a thin glass fiber of 3 μm thickness using a small amount of acetone-soluble bond glycol-phthalate and placed in the Gandolfi camera. The sample particle was exposed to a monochromated synchrotron X-ray with a wavelength of 2.161 ± 0.001 Å and a diameter of 0.3 mm. The exposure duration is 3 h for cometary particles. The X-ray diffraction pattern was recorded on a high-resolution imaging plate (Fuji film BAS SR2040) and the pattern was transformed to an 8-bit TIF image by using an imaging plate reader (Fuji film BAS 2500). The diffraction angle resolution is 0.05 degree. The multiple diffraction rings on the image are converted to a powder X-ray diffraction pattern using software that we developed. Determination of interlayer spacings, integrated intensities of reflections, and identification of minerals were performed using the software.

The analyses were performed at beam line 3A of the Photon Factory Institute of Material Science, High Energy Accelerator Research Organization (KEK) and at beam line BL37XU of Japan Synchrotron Radiation Research Institute (SPring-8). The Gandolfi camera (Gandolfi 1967) is a unique apparatus that enables us to obtain a powder X-ray diffraction pattern from a small particle 5–300 μm in diameter. The measurable size range perfectly matches diameters of cometary dust and cosmic dust such as interplanetary dust particles and micrometeorites. In addition, this method is most useful for identification of minerals and determination of relative mineral abundance for a particle with multiple mineral phases, because deconvolution of reflections is not difficult for powder diffraction patterns. Thus the method has been applied for characterization of bulk mineralogy of individual cosmic dust and small dust aggregates from primitive chondrites (Nakamura et al. 2001; Noguchi et al. 2002; Nakamura 2006).

Synchrotron X-ray Microtomography and Electron Microscopy

Following X-ray diffraction analysis, individual particles were imaged and analyzed by scanning electron microscopes equipped with energy-dispersive spectrometer (SEM/EDS) at

NASA JSC and at Kyushu University (Nakamura 2006; Zolensky et al. 2006). After SEM analysis, two particles (C2054,13,35,81,0 and C2054,13,35,82,0) were embedded in epoxy resin and ultramicrotomed to make flat surfaces by using Leica-Reichert Supernova Ultramicrotome at Ibaraki University (Noguchi et al. 2002). After ultramicrotomy, the flat surfaces of the two particles were observed by a field-emission scanning electron microscope (FE-SEM: JEOL JSM-7000F) at the University of Tokyo. Major element concentrations were also obtained by using an electron probe microanalyzer (EPMA: JEOL JXA-733 superprobe) at Kyushu University.

Four cometary particles (C2004,1,44,3,0, C2054,0,35,4,0, C2054,0,35,5,0, and C2054,0,35,6,0) were imaged and analyzed by imaging microtomography using a Fresnel zone plate (Uesugi et al. 2006) at beam line BL47XU of SPring-8 (Uesugi et al. 2003). The imaging experiments were made using an 8 keV X-ray approximately 30 × 30 μm in size with 3600 projections/180 degrees for each slice. Three-dimensional structures were obtained from 482–686 slice images (1035 × 1035 pixels) using the convolution back projection for projection methods (Tsuchiyama et al. 2005) with a voxel (pixel in 3-D) size of 42.5 × 42.5 × 42.5 nm, which gives effective spatial resolution of a few 100 nm. The Mg/(Mg + Fe) ratios of olivine and pyroxene were estimated from the linear attenuation coefficients (LACs) observed in the CT images using an empirical relation between observed and theoretical LACs (Tsuchiyama et al. 2005). The solid portion (whole grain including everything but atmosphere) and the highly absorbed portion that might correspond to silicates and FeS or Fe metal phases were obtained by thresholding the CT-image contrast. Three-dimensional image processing and analysis, including thresholding, mode calculation, and external shape drawing (bird's eye view images of particles) were performed by Slice software (Nakano et al. 2006).

RESULTS AND DISCUSSION

Track Features

Track 35, from which 25 out of 28 particles were extracted, has a bulbous structure in the front part, and the remaining portion is a narrow tunnel leading to the terminal particle (Fig. 1a). The wide bulbous structure indicates that the incoming particle was exploded upon impact due to instantaneous ejection of volatile materials (Tsuchiyama et al. 2007). The sudden pressure increase during the explosion in aerogel produced a high density of cracks perpendicular to both the top surface and the bulb walls. Most material of the incoming particle appears to have been disaggregated and spread over the walls. Only some particles survived the explosion, kept moving deeper in the aerogel, and stopped at the end of the subtracks and the main track. Such particles are defined as terminal particles. Among 25 particles investigated, two particles are from the terminal, one from position C, and the other from position I. The remaining 23 particles are those extracted from the wall of the bulbous portions (Figs. 1b and 1c; Table 1). On the other hand, the whole structure of Track 44 is not well documented because it is still in the aerogel cell. But, judging from stereoscope observation of the surface of the cell, the Track 44 also has a large bulbous portion suggestive of explosion of an incoming particle. The three particles analyzed in this study are taken from the wall of the bulbous portion.

Mineralogical, Structural, and Compositional Features

Synchrotron X-ray diffraction and microtomography analyses were performed on individual Wild 2 particles and the results are summarized along with particle size, morphology, and composition in Table 1. The size of the particles analyzed ranges from 5 × 4 to 25 × 20 μm. Most particles are irregular in shape, but some are subrounded. Based on EDS spectra, many particles show chondritic elemental abundance except for some particles that are either enriched or depleted in both Fe and S. X-ray diffraction analysis revealed that Stardust particles show only two types of diffraction patterns: highly crystalline and almost amorphous. Therefore, we classified the particles into crystalline and amorphous-rich types.

Crystalline Type Wild 2 Particles

We identified three crystalline particles, all of which were recovered from Track 35 (Table 1). The three particles are relatively large, measuring 20 μm or larger in the longest dimension. Three particles were found from different locations in Track 35: C2054,0,35,6,0 is from the terminal of a subtrack, C2054,0,35,4,0 is from the wall of a bulbous portion, and C2054,0,35,49,0 is from the wall of a narrow track close to the terminal particle of the main-track (Figs. 1c, 1d; Table 1). The most characteristic feature of this type is that all mineral phases in the particle including silicates, Fe sulfide, and Fe metal are well crystallized.

The first crystalline particle is C2054,0,35,6,0. This is a terminal particle of a small subtrack. It is an essentially non-porous material consisting of olivine, low-Ca pyroxene, and kamacite several microns in size (Figs. 2a–c). Reflections of both silicates and metal in the diffraction pattern are very sharp, suggestive of high degrees of crystallinity (Fig. 2c). Both olivine and pyroxene are estimated to be enriched in Mg, because the interlayer spacings, which are determined from the diffraction angles, are much closer to Mg-rich end-members (forsterite and enstatite) than Fe-rich ones. Based on the (130) spacing of olivine and a determinative curve between Fo# and the (130) spacing (Yoder and Sahama 1957), Fo# in this particle is estimated to be 81.9 ± 1.5. The Fo# estimated from the LACs in the CT images is 78 ± 2. CT images (Figs. 2a, 2b, and 3) suggest that the particle shows poikilitic or porphyritic texture characteristic for igneous

Table 1. Summary of the results of X-ray diffraction, microtomography, and SEM analysis.

Official JSC number	Track position	Particle type	Mineral composition	Size (μm)	Morphology	SEM chemical composition
Allocation in February 2006						
C2054,0,35,8,0	Not analyzed yet					
C2054,0,35,7,0	Track 35 position A	Amorphous-rich	Amorphous and a phase unidentified	7 × 5	Irregular	Chondritic
C2004,1,44,3,0[a]	Track 44	Amorphous-rich	Amorphous, FeSi metal, and an unidentified phase	20 × 15	Irregular	
C2004,1,44,2,0	Track 44	Amorphous-rich	Amorphous-rich, FeSi metal, and Fe sulfide	20 × 15	Irregular	Chondritic
C2004,1,44,1,0	Track 44	Amorphous-rich	Amorphous and FeSi metal	20 × 15	Irregular	Chondritic
C2054,0,35,6,0[a] (TP)	Track 35 position C	Crystalline	Olivine, low-Ca pyroxene and kamacite	20 × 15	Irregular	
C2054,0,35,5,0[a]	Track 35 position B	Amorphous-rich	Amorphous, FeSi metal, and Fe sulfide	25 × 20	Subrounded	Chondritic
C2054,0,35,4,0[a]	Track 35 position B	Crystalline	Olivine, low- and high-Ca pyroxene, and plagioclase	20 × 15	Irregular	FeS-poor Mg-rich
Allocation in March 2006						
C2054,10,35,60,0	Track 35 position D	Amorphous-rich	Amorphous-rich, FeSi metal, and Fe sulfide	20 × 20	Subrounded	Chondritic
C2054,10,35,61,0	Track 35 position D	Amorphous-rich	Amorphous-rich, FeSi metal, and Fe-sulfide	10 × 10	Irregular	Chondritic
C2054,11,35,62,0 (TP)	Track 35 position I	Amorphous-rich KS-crystalline	Amorphous, kamacite, taenite, Fe sulfide, and trace of low-Ca pyroxene	15 × 10	Irregular	Chondritic
C2054,14,35,63,0	Track 35 position F	Amorphous-rich	Amorphous-rich, FeSi metal, Fe sulfide, and probably olivine	10 × 10	Irregular	FeS-rich Mg-poor
C2054,14,35,64,0	Track 35 position F	Amorphous-rich	Amorphous-rich, FeSi metal, and Fe sulfide	6 × 6	Subrounded	FeS-rich Mg-poor
C2054,15,35,65,0	Track 35 position E	Amorphous-rich KS-crystalline	Amorphous, kamacite, taenite, and Fe sulfide	15 × 15	Subrounded	Chondritic
C2054,15,35,66,0	Not analyzed yet			7 × 5	Irregular	Chondritic
C2054,15,35,67,0	Track 35 position E	Amorphous-rich	Amorphous dominant	8 × 8	Irregular	Chondritic
C2054,15,35,68,0	Track 35 position E	Amorphous-rich	Amorphous-rich, FeSi metal, and Fe sulfide	10 × 10	Irregular	Chondritic
C2054,15,35,69,0	Track 35 position E	Amorphous-rich	Amorphous-rich, FeSi metal, and Fe sulfide	8 × 8	Subrounded	Chondritic
C2054,15,35,70,0	Track 35 position E	Amorphous-rich	Amorphous dominant	8 × 8	Subrounded	FeS-rich Mg-poor
C2054,15,35,71,0	Track 35 position E	Amorphous-rich	Amorphous-rich, FeSi metal, and Fe sulfide	15 × 10	Irregular	Chondritic
C2054,15,35,72,0	Track 35 position E	Amorphous-rich	Amorphous-rich, FeSi metal, Fe sulfide, and probably low-Ca pyroxene	10 × 10	Irregular	Chondritic
C2054,16,35,73,0	Track 35 position G	Amorphous-rich	Amorphous-rich, FeSi metal, and Fe sulfide	5 × 4	Irregular	Chondritic
C2054,16,35,74,0	Track 35 position G	Amorphous-rich	Amorphous-rich, FeSi metal, and Fe sulfide	10 × 10	Irregular	Chondritic
C2054,16,35,75,0	Not analyzed yet			8 × 8	Irregular	Chondritic
C2054,16,35,76,0	Track 35 position G	Amorphous-rich	Amorphous-rich, FeSi metal, and Fe sulfide	10 × 10	Irregular	Chondritic
C2054,16,35,77,0	Not analyzed yet			8 × 8	Irregular	Chondritic
C2054,16,35,78,0	Not analyzed yet			7 × 7	Irregular	Chondritic
C2054,17,35,79,0	Track 35position H	Amorphous-rich	Amorphous-rich, FeSi metal, Fe sulfide, and probably olivine	8 × 8	Irregular	Chondritic

Table 1. *Continued.* Summary of the results of X-ray diffraction, microtomography, and SEM analysis.

Official JSC number	Track position	Particle type	Mineral composition	Size (μm)	Morphology	SEM chemical composition
C2054,17,35,80,0	Track 35 position H	Amorphous-rich	Amorphous-rich and FeSi metal	10 × 7	Subrounded	Chondritic
C2054,13,35,81,0	Track 35 position K	Amorphous-rich	Amorphous-rich, FeSi metal, and Fe sulfide	25 ×15	Irregular	Chondritic
C2054,13,35,82,0	Track 35 position K	Amorphous-rich	Amorphous-rich, FeSi metal, and Fe sulfide	20 × 10	Irregular	Chondritic
Allocation in May 2006						
C2054,0,35,45,0	Track 35 position J	Amorphous-rich	Amorphous dominant		Irregular	
C2054,0,35,46,0	Track 35 position J	Amorphous-rich	Amorphous-rich, FeSi metal, and Fe sulfide	20 × 20	Irregular	
C2054,0,35,47,0	Track 35 position J	Amorphous-rich	Amorphous dominant		Irregular	
C2054,0,35,49,0	Track 35 position J	Crystalline	Mg-rich olivine, low-Ca pyroxene, and kamacite	20 × 8	Irregular	

TP: Terminal particle.

[a]Particles imaged by microtomography.

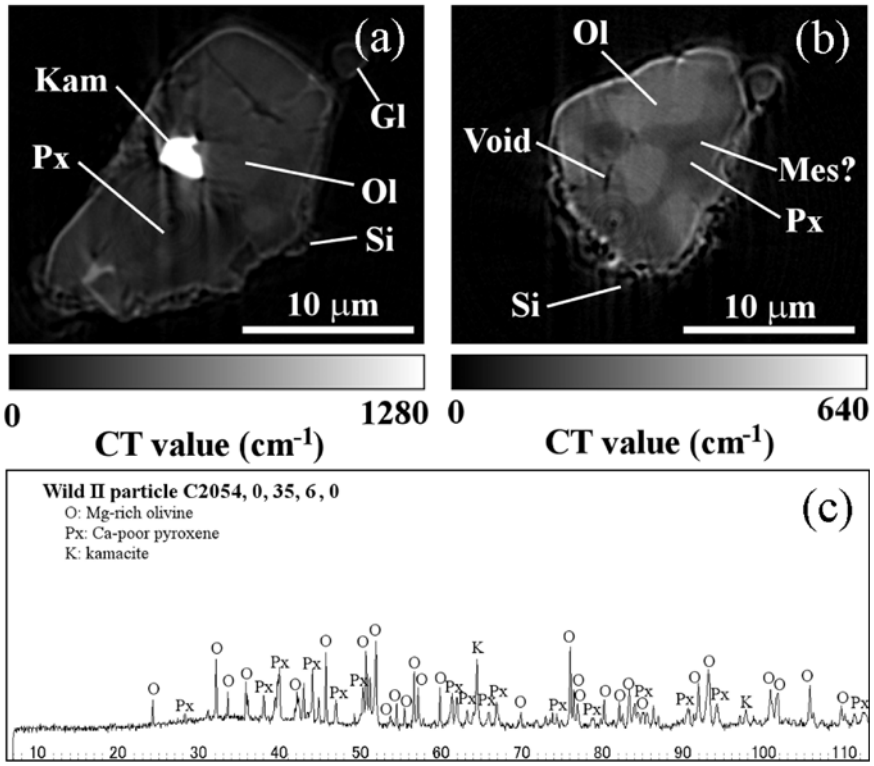

Fig. 2. Crystalline particle C2054,0,35,6,0. a) and b) Micro-tomography images, showing that the particle consists of olivine (Ol), low-Ca pyroxene (Px), kamacite (K) of several microns in size. Light and dark objects correspond to materials with high and low linear attenuation coefficients (CT values), respectively, as shown by the gray scale on the bottom. Small amounts of mesostasis (Mes?) seem to be present. A small void is also seen. The particle is surrounded by silica aerogel (Si). Gl is a glass fiber for holding the particle with glue, which is not well recognized in the images. Bright lines on the surface are artifacts due to the refraction of X-ray beams. c) Synchrotron X-ray diffraction pattern, showing the particle is crystalline. Horizontal scale is 2θ diffraction angle.

rocks: euhedral to subhedral olivine phenocrysts are surrounded by low-Ca pyroxene (see Appendix). The textures require partial melting of pre-existing solids. In addition, the texture is very similar to the microporphyritic texture commonly observed in chondrules. Successive CT images (Fig. 3) show that this particle is essentially non-porous igneous material (a very small amount of voids are seen; Fig. 2b) and Fe metal is enclosed within silicates. The modal abundance of minerals was estimated from a three-dimensional image: 53, 46, and 1 vol% for low-Ca pyroxene, olivine, and kamacite, respectively. The particle is covered with silica aerogel. The boundary between the particle and aerogel is discrete, as is observed in slice images from 330 to 430 (Fig. 3) where a piece of melted

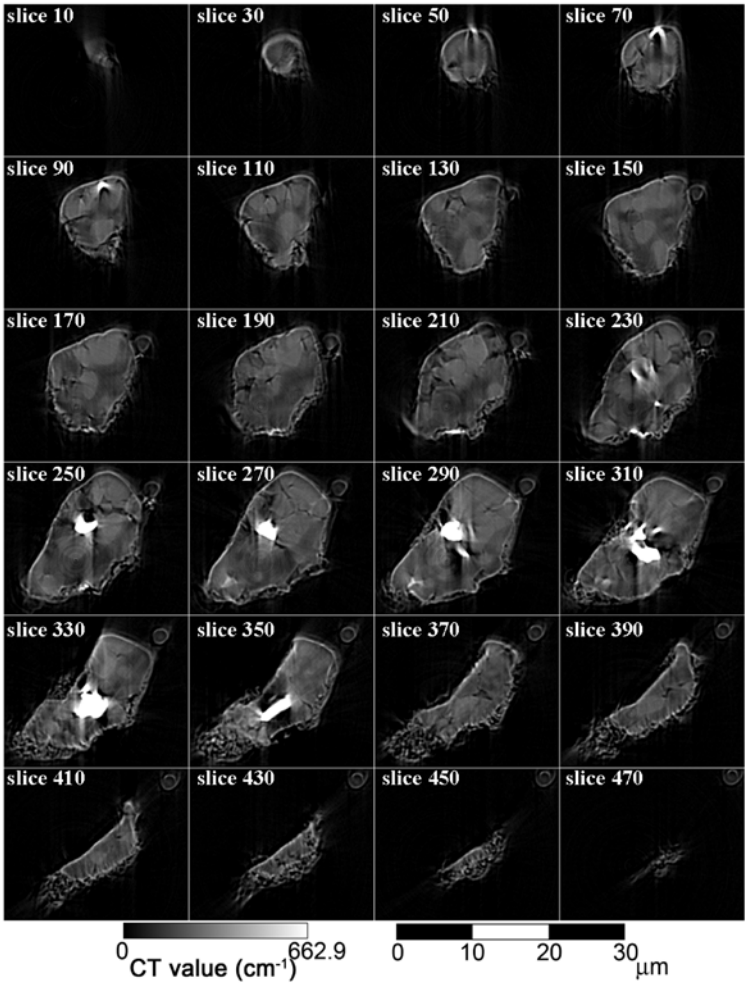

Fig. 3. Successive micro-tomography image of crystalline particle C2054,0,35,6,0. A kamacite grain is completely included within silicates based on the slice images from 250 to 350. Silica aerogel and the particle contact with a discrete boundary based on the slice images from 370 to 450. Bright lines on the surface are artifacts due to refraction of X-ray beams. Vertical dark and light bands from kamacite grains are also artifacts due to insufficient X-ray transmission by the kamacite grains.

aerogel, lower left-hand side of the images, is attached to the cometary particle. The sharp boundary between the aerogel and the particle indicates that both materials did not melt together during capture, and thus melting of the particle occurred prior to capture into aerogel.

The second crystalline particle is C2054,0,35,4,0 (Table 1). It has a smooth appearance (Fig. 4a) with small amounts of silica aerogel on the surface and a sharp boundary (Fig. 4b). Like C2054,0,35,6,0, the inside of the particle is filled with coarse silicates (Fig. 4c). Major element abundance is chondritic (CI chondrite elemental abundance), except for depletion of S and Fe (Fig. 4d): in the normal chondritic elemental pattern, large peaks from both S and Fe are observed, because they are among the most abundant elements. Mineral composition is also chondritic: the most abundant mineral is olivine, followed by low- and high-Ca pyroxenes, and minor amounts of plagioclase (Fig. 4e). Olivine and pyroxene have high Mg/Fe ratios, which is inferred from interlayer spacing (Fig. 4e), LACs in CT images and chemical composition (Fig. 4d). Fo# is 87.9 ± 1.5 estimated from the (130) spacing of olivine and 87 ± 4 from the LACs of CT images. CT images suggest that the particle is composed of a small number of grains of olivine and pyroxene (~90 vol%) with plagioclase-like material (~10 vol%) (Fig. 4c) (see Appendix). A very small number of voids are seen. A part of the surface has a high density of surface features indicating abrasion or breakage, implying that the particle was fractured probably during the entry into the aerogel (Fig. 4b). The third crystalline particle is C2054,0,35,49,0 which is located in a narrow tunnel to the terminal particle (position J in Fig. 1c). This particle also gives sharp reflections of olivine, low-Ca pyroxene, and kamacite (Fig. 5).

Amorphous-Rich Type Wild 2 Particles

Except for the three crystalline particles, Wild 2 particles are classified to this type. Most of the particles extracted from the wall of bulb in both Tracks 35 and 44

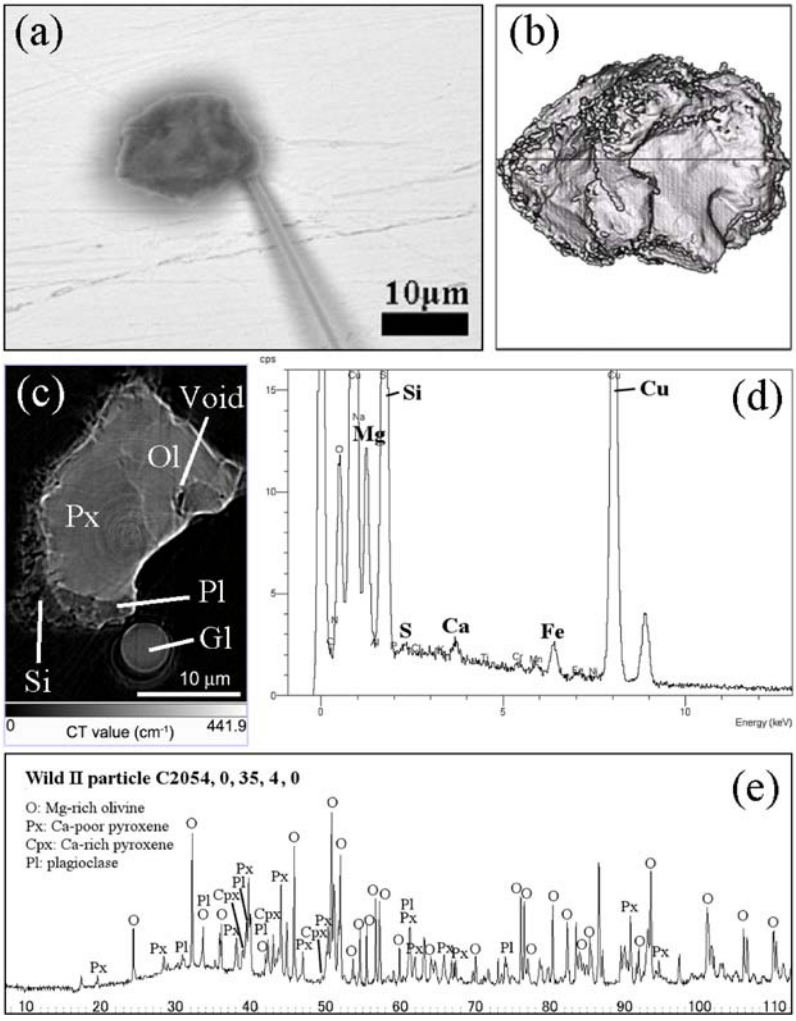

Fig. 4. Crystalline particle C2054,0,35,4,0. a) BSE image. The particle shows a smooth surface fixed on top of a thin glass fiber 3 μm in diameter. A bird's-eye view image of the particle constructed from 3-D CT images. Some aerogel on the surface was removed by the image processing technique, but some remained as seen by the lumpy texture. The smooth surface on the front seems to be a fracture. c) Microtomography image, showing the particle consists mostly of olivine and pyroxene. Light and dark objects correspond to materials with high and low linear attenuation coefficients (CT values), respectively, as shown by a gray scale on the bottom. The dark material at the bottom of the particle is probably plagioclase. Gl is a glass fiber for holding the particle with glue, which is seen around the fiber. Bright lines on the surface are artifacts due to the refraction of X-ray beams. d) EDS spectrum, showing that the particle has a chondritic composition, but depleted in S and Fe. Cu comes from substrate Cu plate. e) X-ray diffraction pattern. Horizontal scale is 2θ diffraction angle.

belong to this type, but one terminal particle from position I in Track 35 is also this type. Characteristics of this type are: 1) high concentrations of Mg, S, and Fe in roughly chondritic abundance, and 2) missing or very weak silicate diffraction lines. The high Mg content is inconsistent with a very low abundance of crystalline silicates because Mg is usually contained in silicates such as olivine and pyroxene in primitive chondritic material. This discrepancy suggests that Mg is contained in amorphous silicates in this type of particles. Most amorphous-rich particles show very broad reflections of Fe sulfide and Fe metal, suggesting that these minerals are also poorly crystalline. But some of the particles give very sharp reflections of Fe sulfide and Fe metal, although silicate reflections are missing or very weak. This type of particle constitutes a small subtype in the amorphous-rich type and is hereafter referred to as kamacite and sulfide (KS) crystalline.

Amorphous-rich particle C2054,11,35,62,0 is a terminal particle of a small subtrack (position C in Fig. 1b). It shows a rough surface (Fig. 6a) and has solar elemental abundance except for high abundance of Si (Fig. 6b). Close inspection using SEM/EDS revealed that the surface of this particle is covered with small blocks of silica aerogel. The X-ray diffraction pattern indicates that the major crystalline materials are pyrrhotite, kamacite, and taenite with a small amount of low-Ca pyroxene (Fig. 6c), thus the particle is classified as KS crystalline. The low abundance of crystalline silicates (Fig. 6c) irrespective of the high Mg

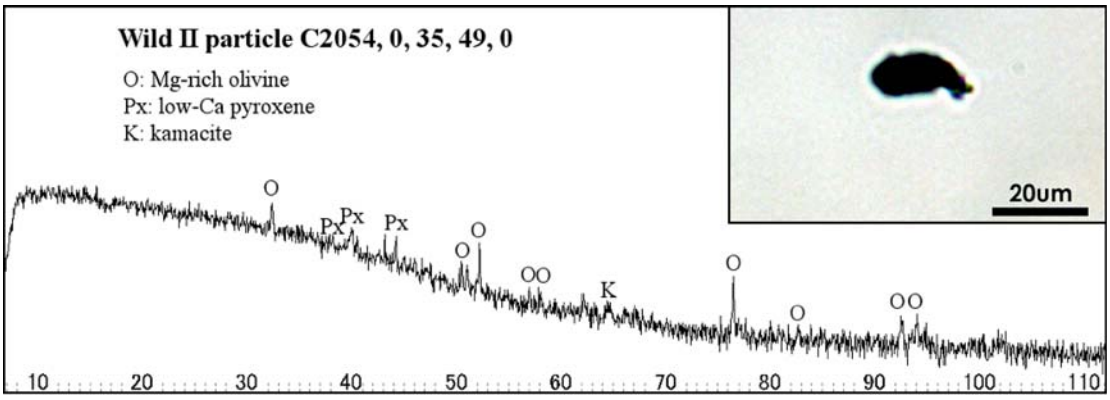

Fig. 5. Synchrotron X-ray diffraction pattern of crystalline particle C2054,0,35,49,0. Although the intensity of reflections from all minerals are weak compared with other two crystalline particles (Figs. 2c and 4e), the shape of reflection is sharp. Horizontal scale is 2θ diffraction angle. Inset: optical photomicrograph of C2054,0,35,49,0 showing long and thin morphology.

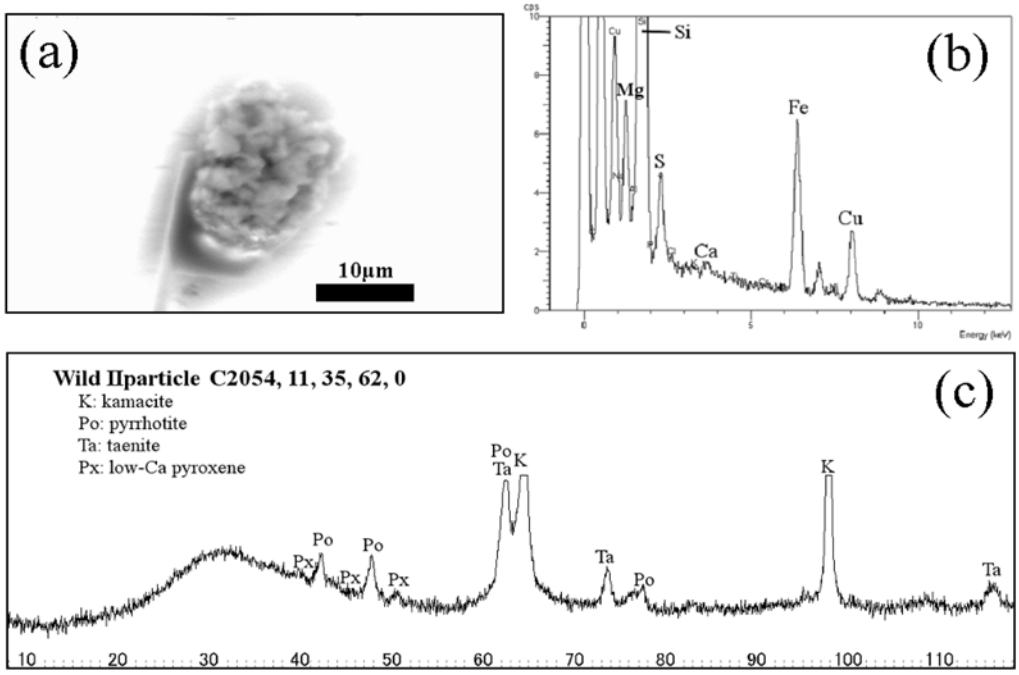

Fig. 6. Amorphous-rich particle C2054,11,35,62,0. (a) BSE image, showing the particle has a rough surface. (b) EDS spectrum, showing that the particle has a chondritic composition. Cu comes from substrate Cu plate. (c) Synchrotron X-ray diffraction pattern. Pyrrhotite and kamacite peaks are large and broad. Horizontal scale is 2θ diffraction angle.

content (Fig. 6b) in this particle suggests the presence of abundant Mg-bearing amorphous silicate. At present, it is unknown how the KS crystalline particles formed and it is also uncertain if they share the same formation process as the rest of the amorphous-rich particles.

The next example of the amorphous-rich type is C2054,0,35,5,0. As shown in Table 1, most of the amorphous-rich type particles, except for two particles of KS crystalline, have mineralogical and compositional features similar to this particle. The particle has a smooth surface, subrounded morphology, and chondritic elemental abundance except for a very high abundance of Si (Figs. 7a and 7b). Unlike KS crystalline particle C2054,11,35,62,0 (Fig. 6a), no aerogel blocks are attached to the surface. Thus the large Si enrichment is attributed to a high Si content in the interior of the particle. Microtomography analysis showed that the particle is a very porous aggregate, having a network structure consisting of numerous voids and probably a mixture of silica aerogel and Wild 2 material (Figs. 7c and 7d), although the aerogel and Wild 2 material are not distinguished in the tomography. The mixing of the aerogel and the indigenous cometary material is consistent with the fact that the particle is extremely enriched in Si (Fig. 7b). The X-ray diffraction pattern indicates that the particle gives broad reflections of Fe

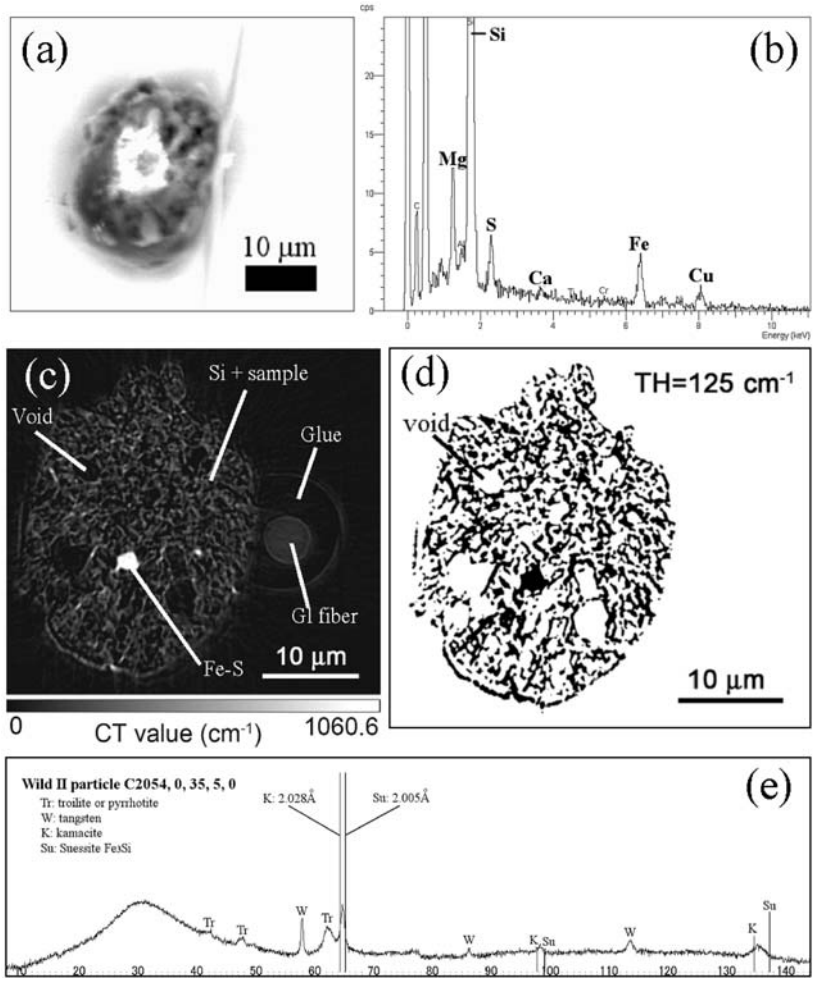

Fig. 7. Amorphous-rich particle C2054,0,35,5,0. a) BSE image showing the particle has a smooth surface. b) EDS spectrum. The particle has a chondritic composition. Cu comes from substrate Cu plate. c) Micro-tomography image. Light and dark objects correspond to materials with high and low linear attenuation coefficients (CT values), respectively, as shown by the gray scale on the bottom. Gl is a glass fiber for holding the particle with glue, which is seen around the fiber. Slightly bright lines on the surface are artifacts due to refraction of X-ray beams. It is a very porous particle, showing network structure consisting of numerous voids and mixtures of cometary material and aerogel. d) Binary image of (c). In this image, void spaces are shown in white. The particle is full of voids. e) Synchrotron X-ray diffraction pattern. Broad suessite $FeSi_3$ and sulfide peaks are observed. Kamacite peak positions are also indicated for comparison. Tungsten peaks come from a small piece of tungsten needle contaminated during particle extraction, which is confirmed by the microtomography. Horizontal scale is 2θ diffraction angle.

sulfide and Fe metal and no silicate reflections, suggesting that the metal and the sulfide are poorly crystalline and silicates are amorphous. This fact reinforces the interpretation that the material consisting network structure (Fig. 7c) is amorphous. The subrounded morphology, the presence of voids, and the mixing between aerogel and Wild 2 material strongly suggest that the particle formed during a brief melting during capture into aerogel.

The interlayer spacing of Fe metal in this particle shows a slight shrinkage. This is probably due to incorporation of metallic Si into Fe, which induces overall downsizing of unit cell. In the X-ray diffraction pattern (Fig. 7e), the positions of reflections from Fe-metal kamacite and Fe_3Si suessite (Keil et al. 1982) are shown. Suessite consistently yields diffraction peaks at angles higher than kamacite, since the suessite unit cell is smaller than kamacite by approximately 1% due to substitution of Fe by the smaller Si atom. The reflections from this particle appear between kamacite and suessite (Fig. 7e). We can interpret that certain amounts of Si are present in metallic Fe in this particle. Main Si supplier is aerogel, because it is made of almost pure SiO_2. During high temperature melting upon impact, SiO_2 was melted and reduced to form metallic Si, due to extremely low oxygen fugacity in space. The metallic Si was mixed with metallic iron, and rapidly solidified to form an amorphous-rich type particle. The presence of Si-bearing metallic Fe is common only in the amorphous-rich type particles, except for KS crystalline, based on the results of our X-ray diffraction. In addition, further evidence was obtained from analysis of amorphous-rich type particle C2004,1,44,3,0 for which X-ray

diffraction, micro-tomography, and transmission electron microscopy (TEM) were performed (Rietmeijer et al. 2007). The particle showed a void-rich porous internal texture based on the CT image and gave metallic Fe X-ray diffractions matching well with suessite. Subsequent TEM observation confirmed the presence of suessite from electron diffraction and chemical composition (see Rietmeijer et al. 2008 for detailed description).

The presence of suessite and the absence of crystalline silicates in most of amorphous-rich type particles suggest that they were melted with silica aerogel upon capture impact. In order to demonstrate the interpretation, observation of internal texture and analysis of major element abundance were carried out on two amorphous-rich type particles, C2054,13,35,81,0 and C2054,13,35,82,0. Textural observation by FE-SEM (Figs. 8a and 8b) showed that the two particles are extensively vesiculated and contain many small round inclusions, probably suessite and/or sulfides. The texture indicates that the particles were entirely melted and cooled rapidly. No relict silicate grains were detected during FE-SEM observation. Major element analysis using an electron-probe analyzer (Fig. 8c) showed that the two particles have compositions close to solar elemental abundance except for a large enrichment of SiO_2. This demonstrates that the particles were melted together with silica aerogel. Compared with solar abundance, Si content in the two particles is enriched by one order of magnitude, suggesting that the Wild 2 particles and silica aerogel were mixed with a ratio of 1:10, respectively. Incorporation of large amounts of the silica component is likely to promote formation of SiO_2-rich glass and prevent rapid crystallization of olivine and pyroxene.

Significance of the Presence of Crystalline Particle in Comet Wild 2

Our synchrotron X-ray diffraction and tomography analyses showed that Wild 2 particles are classified into two types based on the silicate crystallinity. Amorphous-rich type particles, except for KS crystalline, were products of melting during capture (Fig. 8). Two KS crystalline particles were found. They probably are partially melted materials because weak diffractions of silicates were detected (Fig. 6). Indigenous fine-grained amorphous materials that were produced by a variety of amorphitization process in interstellar space such as radiation and particle bombardment may be preserved in the KS crystalline particles. For that, further detailed observation using TEM is required.

With the exception of the two KS crystalline-type particles, there do not seem to be intermediate ones that have a crystal/amorphous ratio of ~1, at least among the silicates. One possible interpretation is that the large initial particle that produced Track 35 was made of only two types of material: non-porous coarse crystalline material and very porous fine-grained material. The former survived melting at capture

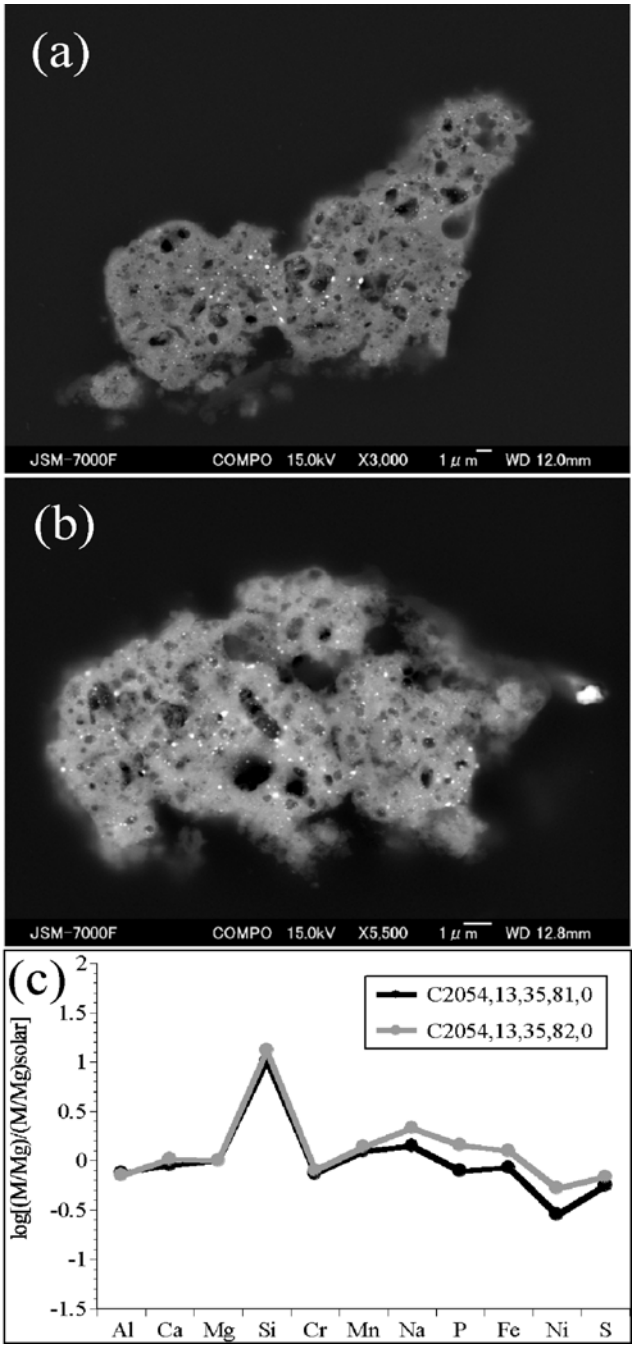

Fig. 8. Internal texture and major element abundance of the amorphous-rich type particles, C2054,13,35,81,0 and C2054,13,35,82,0. a) BSE image of C2054,13,35,81,0 taken by FE-SEM. Numerous void spaces with diameter of 1 μm or less are observed throughout the particle. No relict silicates that escaped melting were found in the FE-SEM observation. Tiny bright inclusions are also dispersed in the particle. They are probably FeSi-metal and Fe-sulfides based on the synchrotron X-ray diffraction of the whole particle (Table 1). b) BSE image of C2054,13,35,82,0. The texture is very similar to that of (a). c) Major element abundance of the two particles, taken by EPMA. Both particles have similar element abundance close to solar, except for a large Si enrichment and small Ni and S depletions.

impact and recovered as crystalline-type particles, while the latter was severely melted at impact and recovered as amorphous-rich type particles. The latter might have been an aggregate of small grains that have solar elemental abundance as a whole because the recovered amorphous-rich particles have compositions close to solar abundance (Fig. 8c).

On the other hand, clearly crystalline particles maintain the records of comet Wild 2 because they have not melted during capture. The igneous texture observed in C2054,0,35,6,0 (Figs. 2a and 2b) suggests that the particle experienced a high-temperature heating episode prior to capture. Although in-situ melting in the comet cannot be ruled out, the high-temperature heating occurred probably prior to formation of the comet (e.g., Zolensky et al. 2006), because the presence of volatile compounds (ices) that degas at low temperature to form the coma of Wild 2 is not consistent with high-temperature (>1000 K) processing of rock-forming minerals on Wild 2 at any time in its history.

Here we estimate the temperature to which crystalline particle C2054,0,35,6,0 was heated during formation. Based on the results of X-ray diffraction (Fig. 2c) and microtomography (Fig. 3), both olivine and low-Ca pyroxene are enriched in Mg and the mode of occurrence is 46 and 53 vol%, respectively. The phase diagram of forsterite and silica system (Bowen and Anderson 1914) is applied for temperature estimation with assumptions that olivine and low-Ca pyroxene in the particle are rich in Mg and no third component such as high-Ca pyroxene is entirely absent. Using bulk composition of the particle obtained from the mode of occurrence of olivine and pyroxene, temperature required for the formation of this crystalline particle can be estimated. When the temperature increases, low-Ca pyroxene starts melting at approximately 1550 °C, and at higher temperature forsterite starts melting. Finally, around 1700 °C, the particle was totally melted. On the other hand, the particle exhibits a poikilitic or porphyritic texture (Figs. 2a and 2b). This suggests that low-Ca pyroxene was melted during formation, but it is likely that olivine was not completely melted. Therefore, it is concluded that the crystalline cometary dust C2054,0,35,6,0 has been heated to temperature between 1550 and 1700 °C. At this temperature range, Fe metal in the particle (Fig. 2a) was also melted, considering its melting temperature (1540 °C).

CONCLUSIONS

Wild 2 particles can be classified into only two types: crystalline and amorphous-rich. No intermediate types (like fine-grained types of IDPs) have been found so far in our study. Crystalline and amorphous-rich type particles are easily distinguished by X-ray diffraction and micro-tomography in a non-destructive way. Crystalline type occurs in 3 out of 28 particles and the rest are amorphous-rich type. Since most particles analyzed in the present study are from type B Track 35, the crystalline/amorphous-rich ratio may change in different types of tracks. Crystalline-type particles formed at a high temperature probably prior to formation of the comet, while most of the amorphous-rich type particles formed by melting during capture. In our analysis, no phyllosilicates and carbonates have been found so far in cometary dust.

Acknowledgments—We thank Drs. Iwazumi, Koyama, and Mori at KEK and Drs. Terada and Takagaki at SPring-8 for technical support during X-ray diffraction and microtomography analysis, Drs. Zolensky and Nakamura-Messenger for valuable support during clean room work at NASA Johnson Space Center, Drs. Nagahara, Tachibana, and Yoshida for technical support during FE-SEM analysis, Drs. Sandford, Ebel, and an anonymous referee for the review, and Dr. Okazaki, Messrs. Yokoyama, Murata, Okazaki, and Miss Sakamoto for the help during analyses at synchrotron facilities. Tomoki Nakamura and Akira Tsuchiyama were supported by a Grant-in-aid of the Japan Ministry of Education, Culture, Sports, Science and Technology.

Editorial Handling—Dr. Scott Sandford

REFERENCES

Bowen N. L. and Anderson O. 1914. The binary system MgO-SiO_2. *American Journal of Science* 37:487–500.

Brownlee D. E., Tsou P., Aléon J., Alexander C. M. O' D., Araki T., Bajt S., Baratta G. A., Bastien R., Bland P., Bleuet P., Borg J., Bradley J. P., Brearley A., Brenker F., Brennan S., Bridges J. C., Browning N. D., Brucato J. R., Bullock E., Burchell M. J., Busemann H., Butterworth A., Chaussidon M., Cheuvront A., Chi M., Cintala M. J., Clark B. C., Clemett S. J., Cody G., Colangeli L., Cooper G., Cordier P., Daghlian C., Dai Z., D'Hendecourt L., Djouadi Z., Dominguez G., Duxbury T., Dworkin J. P., Ebel D. S., Economou T. E., Fakra S., Fairey S. A. J., Fallon S., Ferrini G., Ferroir T., Fleckenstein H., Floss C., Flynn G., Franchi I. A., Fries M., Gainsforth Z., Gallien J.-P., Genge M., Gilles M. K., Gillet P., Gilmour J., Glavin D. P., Gounelle M., Grady M. M., Graham G. A., Grant P. G., Green S. F., Grossemy F., Grossman L., Grossman J. N., Guan Y., Hagiya K., Harvey R., Heck P., Herzog G. F., Hoppe P., Hörz F., Huth J., Hutcheon I. D., Ignatyev K., Ishii H., Ito M., Jacob D., Jacobsen C., Jacobsen S., Jones S., Joswiak D., Jurewicz A., Kearsley A. T., Keller L. P., Khodja H., Kilcoyne A. L. D., Kissel J., Krot A., Langenhorst F., Lanzirotti A., Le L., Leshin L. A., Leitner J., Lemelle L., Leroux H., Liu M.-C., Luening K., Lyon I., MacPherson G., Marcus M. A., Marhas K., Marty B., Matrajt G., McKeegan K., Meibom A., Mennella V., Messenger K., Messenger S., Mikouchi T., Mostefaoui S., Nakamura T., Nakano T., Newville M., Nittler L. R., Ohnishi I., Ohsumi K., Okudaira K., Papanastassiou D. A., Palma R., Palumbo M. E., Pepin R. O., Perkins D., Perronnet M., Pianetta P., Rao W., Rietmeijer F. J. M., Robert F., Rost D., Rotundi A., Ryan R., Sandford S. A., Schwandt C. S., See T. H., Schlutter D., Sheffield-Parker J., Simionovici A., Simon S., Sitnitsky I., Snead C. J., Spencer M. K., Stadermann F. J., Steele A., Stephan T., Stroud R., Susini J., Sutton S. R., Suzuki Y., Taheri M., Taylor S., Teslich N., Tomeoka K., Tomioka N., Toppani A., Trigo-Rodríguez J. M., Troadec D., Tsuchiyama A., Tuzzolino A. J., Tyliszczak T., Uesugi K.,

Velbel M., Vellenga J., Vicenzi E., Vincze L., Warren J., Weber I., Weisberg M., Westphal A. J., Wirick S., Wooden D., Wopenka B., Wozniakiewicz P., Wright I., Yabuta H., Yano H., Young E. D., Zare R. N., Zega T., Ziegler K., Zimmerman L., Zinner E., and Zolensky M. 2006. Comet 81P/Wild 2 under a microscope. *Science* 314:1711–1716.

Ebel D. S., Mey J. L., and Rivers M. L. 2007. Nondestructive laser confocal scanning microscopy and synchrotron microtomography of single Stardust and analog tracks in aerogel keystones (abstract #1977). 38th Lunar and Planetary Science Conference. CD-ROM.

Flynn G., Bleuet P., Borg J., Bradley J. P., Brenker F., Brennan S., Bridges J. C. Brownlee D. E., Bullock E., Burghammer M., Clark B. C., Dai Z. R., Daghlian C. P., Djouadi Z., Fakra S., Ferroir T., Floss C., Franchi I. A., Gainsforth Z., Gallien J.-P., Gillet P., Grant P. G., Graham G. A., Grossemy F., Heck P., Herzog G. F., Hoppe P., Hörz F., Huth J., Igantyev K., Ishii H., Janssens K., Joswiak D., Kearsley A. T., Khodja H., Lanzirotti A., Leitner J., Lemelle L., Leroux H., Luening K., MacPherson G., Marhas K., Matrajt G., Nakamura T., Nakamura-Messenger K., Nakano T., Newville M., Papanastassiou D. A., Pianetta P., Rao W., Riekel C., Rietmeijer F., Rost D., Schwandt C. S., See T. H., Sheffield-Parker J. A., Simionovici S., Sitnitsky S. I., Snead C. J., Stadermann F. J., Stephan T., Stroud R. M., Susini J., Suzuki Y., Sutton S. R., Taylor S., Teslich N., Troadec D., Tsou P., Tsuchiyama A., Uesugi K., Vekemans B., Vicenzi E., Vincze L., Westphal A. J., Wozniakiewicz P. A., Zinner E., and Zolensky M. 2006. Elemental compositions of comet 81P/Wild 2 samples collected by Stardust. *Science* 314: 1731–1735.

Gandolfi G. 1967. Discussion upon methods to obtain X-ray powder patterns from a single crystal. *Mineralogica et Petrographica Acta* 13:67–74.

Hörz F., Bastien, R., Borg J., Bradley, J. P., Bridges J. C., Brownlee D. E., Burchell M. J., Cintala M. J., Dai Z. R., Djouadi Z., Dominguez G., Economou T. E., Fairey S. A. J., Floss C., Franchi I. A., Graham G. A., Green S. F., Heck H., Hoppe P., Huth J., Ishii H., Kearsley A. T., Kissel J., Leitner J., Leroux H., Marhas M., Messenger K., Schwandt C. S., See T. H., Snead S., Stadermann F. J., Stephan T., Stroud R., Teslich N., Trigo-Rodríguez J. M., Tuzzolino A. J., Troadec D., Tsou P., Warren J., Westphal A., Wozniakiewicz P. J., Wright I., and Zinner E. 2006. Impact features on Stardust: Implications for comet Wild 2 dust. *Science* 314:1716–1719.

Keil K., Berkley J. L., and Fuchs L. H. 1982. Suessite, Fe_3Si: A new mineral in the North Haig ureilite. *American Mineralogist* 67:126–131.

Nakamura T., Noguchi T., Yada T., Nakamuta Y., and Takaoka N. 2001. Bulk mineralogy of individual micrometeorites determined by X-ray diffraction analysis and transmission electron microscopy. *Geochimica et Cosmochimica Acta* 65: 4385–4397.

Nakamura T. 2006. Yamato-793321 CM chondrite: Dehydrated regolith material of a hydrous asteroid. *Earth and Planetary Science Letters* 242:26–38.

Nakano T., Tsuchiyama A., Uesugi K., Uesugi M., and Shinohara K. 2006. "Slice" software for basic 3-D analysis. Japan Synchrotron Radiation Research Institute. http://www-bl20.spring8.or.jp/slice. Last accessed February 14, 2008.

Noguchi T., Nakamura T., and Nozaki W. 2002. Mineralogy of phyllosilicate-rich micrometeorites and comparison with Tagish Lake and Sayama meteorites. *Earth and Planetary Science Letters* 202:229–246.

Rietmeijer F. J. M., Nakamura T., Tsuchiyama A., Uesugi K., and Nakano T. 2008. Origin and formation of iron-silicide phases in the aerogel of the Stardust mission. *Meteoritics & Planetary Sciences* 43. This issue.

Tsuchiyama A., Uesugi K., Nakano T., and Ikeda S. 2005. Quantitative evaluation of attenuation contrast of X-ray computed tomography images using monochromatized beams. *American Mineralogist* 90:132–142.

Tsuchiyama A., Nakamura T., Okazaki T., Uesugi K., Nakano T., Akaki T., Iida Y., Jogo K., and Suzuki Y. 2007. Three-dimensional structures and elemental distributions of Stardust impact tracks (abstract #1247). 38th Lunar Planetary Science Conference. CD-ROM.

Uesugi K., Tsuchiyama A., Yasuda H., Nakamura M., Nakano T., Suzuki Y., and Yagi N. 2003. Micro-tomographic imaging for material sciences at BL47XU in SPring-8. *Journal de Physique IV* 104:45–48.

Uesugi K., Takeuchi A., and Suzuki Y. 2006. Development of microtomography system with Fresnel zone plate optics at SPring-8. *Proceedings of SPIE* 6318:63181F, doi: 10.1117/12.679822.

Yoder H. S. and Sahama T. G. 1957. Olivine X-ray determination curve. *American Mineralogist* 42:475–491.

Zolensky M. E., Zega T. J., Yano H., Wirick S., Westphal A. J., Weisberg M. K., Weber I., Warren J. L., Velbel M. A., Tsuchiyama A., Tsou P., Toppani A., Tomioka N., Tomeoka K., Teslich N., Taheri M., Susini J., Stroud R., Stephan T., Stadermann F. J., Snead C. J., Simon S. B., Simionovici A., See T. H., Robert F., Rietmeijer F. J. M., Rao W., Perronnet M. C., Papanastassiou D. A., Okudaira K., Ohsumi K., Ohnishi I., Nakamura-Messenger K., Nakamura T., Mostefaoui S., Mikouchi T., Meibom A., Matrajt G., Marcus M. A., Leroux H., Lemelle L., Le L., Lanzirotti A., Langenhorst F., Krot A. N., Keller L. P., Kearsley A. T., Joswiak D., Jacob D., Ishii H., Harvey R., Hagiya K., Grossman L., Grossman J. N., Graham G. A., Gounelle M., Gillet Ph., Genge M. J., Flynn G., Ferroir T., Fallon S., Ebel D. S., Dai Z. R., Cordier P., Clark B., Chi M., Butterworth A. L., Brownlee D. E., Bridges J. C., Brennan S., Brearley A., Bradley J. P., Bleuet P., Bland P. A., and Bastien R. 2006. Mineralogy and petrology of comet 81P/Wild 2 nucleus samples. *Science* 314:1735–1739.

APPENDIX

Detailed Interpretations of Crystalline Particles Based on Microtomography

In this Appendix, internal structures, or textures, of two crystalline particles (C2054,0,35,6,0 and C2054,0,35,4,0) are discussed based on their CT images. CT images give spatial distribution of linear attenuation coefficients (LACs) as digital images similar to BSE images showing the distribution of backscatter coefficients by SEM (Tsuchiyama et al. 2005). In a BSE image, phases are easily determined or estimated from elemental analysis using a characteristic X-ray (e.g., EDS). In contrast, we cannot obtain such elemental information by tomography. Thus, it is usually difficult to estimate phases from CT images alone. In this study, however, the major phases and their rough proportions were determined by X-ray diffraction. As LACs of the phases are known as a function of the chemical compositions at certain X-ray energy, and the present SR tomography with monochromatic X-ray gives

quantitative information on LACs in the CT images, we can estimate the distribution of the phases, or texture, from the X-ray diffraction information and LAC data.

C2054,0,35,6,0

This particle contains olivine, Ca-poor pyroxene, and kamacite. Kamacite is easily recognized by objects with high LACs of roughly 1850–1900 cm^{-1}, which corresponds to metal of approximately $Fe_{0.8}Ni_{0.2}$–$Fe_{0.9}Ni_{0.1}$ (bright objects in Figs. 2a and 3). The rest of dark region should be composed of olivine and pyroxene. In this region, euhedral or subhedral grains of slightly bright contrast (LAC ~ 240 cm^{-1}) are recognized in the darker matrix (LAC ~ 170 cm^{-1}) (Fig. 2b). If the Mg#(= Mg/(Mg + Fe) × 100) of olivine and pyroxene are similar as almost equilibrated compositions, LAC of olivine is larger than that of Ca-poor pyroxene, and the LAC values correspond to Fo#78 ± 2 for both phases. This corresponds to a portion that seems to have poikilitic texture, where euhedral or subhedral olivine grains are poikilitically enclosed in pyroxene. However, the dark matrix could be heterogeneous with slightly darker regions (indicated as "mes?" in Fig. 2b), which is distinguishable from clearly dark voids. This might be a silica-rich glass or a very fine mixture of glass and other phases (e.g., plagioclase) like mesostasis of a chondrule. These minor phases cannot be recognized by X-ray diffraction. Therefore, we cannot exclude the possibility that this particle has a porphyritic texture rather than a poikilitic texture.

C2054,0,35,4,0

The major phases of this particle are olivine and Ca-poor pyroxene. Plagioclase and a small amount of Ca-rich pyroxene are also detected. The main bright region should consist of olivine and Ca-poor pyroxene (Fig. 4c). This region is divided into two subregions; slightly bright and dark ones with bright boundaries although the LAC values are similar (~170 cm^{-1}). The bright and dark subregions may be olivine (Fo# 87 ± 4) and pyroxene, respectively. The bright boundaries may be enriched in Fe. Plagioclase should be present in dark region (LAC ~ 120–130 cm^{-1}), which is seen in the bottom portion of the particle in Fig. 4c. The plagioclase region could be heterogeneous and might be mesostasis mainly composed of plagioclase crystals. If this is the case, this particle might have a porphyritic texture. However, it should be noted that we cannot determine the texture definitely by the CT images alone. Ca-rich pyroxene should be seen as brighter objects than olivine and Ca-poor pyroxene in CT images, although we cannot recognize this phase clearly.